

***Final Draft***  
**of the original manuscript:**

Paul, J.D.H.; Oehring, M.; Appel, F.; Pyczak, F.:  
**Depth resolved near-surface residual stresses in Gamma-based  
TiAl before and after high temperature exposure**  
In: Intermetallics (2017) Elsevier

DOI: 10.1016/j.intermet.2016.12.014

## **Depth resolved near-surface residual stresses in $\gamma$ -based TiAl before and after high-temperature exposure**

J.D.H. Paul, M. Oehring, F. Appel, and F. Pyczak

Helmholtz-Zentrum Geesthacht, Max-Planck-Str. 1, D-21502 Geesthacht, Germany

Corresponding author: Jonathan Paul, e-mail: [jonathan.paul@hzg.de](mailto:jonathan.paul@hzg.de)

e-mail addresses: [michael.oehring@hzg.de](mailto:michael.oehring@hzg.de); [fritz.appel@hzg.de](mailto:fritz.appel@hzg.de); [florian.pyczak@hzg.de](mailto:florian.pyczak@hzg.de)

### **Abstract**

The aim of this study was to gain an insight into the development of near-surface stress, which has been proposed to play a role in environmental embrittlement, as a function of depth after exposure. Investigations were performed, using both energy and angle-dispersive X-ray diffraction, to determine the residual stress as a function of depth for flat specimens made from two  $\gamma$ -based TiAl alloys in as-polished and exposed (700°C/1 h/air) conditions. It has been found that large compressive stresses are present at the surface of as-polished specimens due to sub-surface deformation that remains despite careful grinding/polishing. After exposure the compressive residual stresses at depths below 0.6  $\mu\text{m}$  are significantly reduced, probably due to the annealing out of deformation induced defects, but remain compressive in nature. However, within 0.6  $\mu\text{m}$  from the outer surface, tensile stresses were present and reached a maximum of around +350 MPa at 0.15  $\mu\text{m}$  depth. The extent to which the development of superficial tensile residual stress and reduced deeper compressive stress contribute to embrittlement remains unclear.

**Keywords:** A. intermetallics. B. residual stresses, surface properties. F. residual stress measurement.

## 1 Introduction

Two-phase titanium aluminide alloys, based on the  $\gamma$  (TiAl) and  $\alpha_2$ (Ti<sub>3</sub>Al) phases, have recently been introduced into the General Electric Genx aero-engine as a high-temperature low-pressure turbine blade material [1]. Nevertheless, one phenomenon that remains relatively unexplained, and is apparently unavoidable, involves the partial or complete loss of room-temperature ductility after elevated-temperature exposure; even after short periods of times or after exposure under argon or vacuum conditions [2, 3]. It has been found that ductility is restored if just a few microns of material are removed from the exposed surface [4-6]. Various investigations have been undertaken to understand the mechanism/s involved. Recently it was proposed that the formation during exposure of a nanometer thick oxygen enriched outer layer (called pre-oxide) is responsible for the embrittlement [5]. It was suggested that this layer imposes a residual tensile stress of up to +250 MPa in the material immediately below the pre-oxide surface. In view of the low fracture toughness, it was thought that this stress was the source of the embrittlement. However, the stress was only determined at an estimated depth of 1 to 2  $\mu\text{m}$  below the surface and the dependence of residual stress on depth was not investigated.

Thus the aim of this paper is to determine how the residual stress varies as a function of depth before and after high-temperature exposure in order to gain possible further insight into the underlying factors that may contribute to the embrittlement mechanism.

## 2 Experimental

In this study two sets of two specimens were prepared. One set of specimens was made from gas atomised powder with a composition of Ti-49Al (at. %) that had been hot isostatically pressed (HIPed) under argon at 1200°C/4 h/200 MPa. Specimens were cut from the HIPed material and

then metallographically prepared by careful grinding followed by vibration polishing using a colloidal silica solution. The second set of specimens was prepared in a similar way from a cast ingot that had been hot extruded to bar (extruded at 1250°C to a 7:1 reduction in cross-sectional area). The composition of this second alloy was Ti-45Al-5Nb-0.2B-0.2C (TNB-V5, also known as Plansee Met-PX). The extrusion direction within these polished/as-exposed specimens was parallel to the direction in which the residual stress was measured, as indicated by  $\sigma$  in Fig. 1. One metallographically prepared specimen from each alloy was exposed to air for one hour at 700°C and then furnace cooled. Such an exposure is known to result in a significant reduction in the ductility of medium-strength alloys and almost complete ductility loss in high-strength alloys [2-6].

The near-surface residual stresses within the as-polished and exposed samples were determined as a function of depth from the outer surface. This was done using both energy and angle-dispersive X-ray diffraction; the experimental set-ups for each of these techniques are shown schematically in Fig. 1.

The energy-dispersive method (Fig. 1a) involved irradiating the sample with a beam of white X-rays that were produced from the bremsstrahlung spectrum of a tungsten tube operating at 60 kV/45 mA. The beam diameter was 0.8 mm and the angle between the incident beam and the flat specimen surface was fixed at 8°. The energy-dispersive technique employs a fixed diffraction angle ( $2\theta$ ) and measures the diffracted beam intensity as a function of X-ray energy. For the set-up employed, a fixed diffraction angle of  $2\theta = 16^\circ$  was used. For each specimen investigated, X-ray diffractograms were recorded for a series of specimen tilt angles (the angle defined by  $\psi$  in Fig. 1) that varied between  $\psi = 0^\circ$  and  $89^\circ$ . From  $\psi = 0^\circ$  to  $70^\circ$ , diffractograms were taken at  $4^\circ$  intervals, then at  $2^\circ$  intervals up to  $\psi = 80^\circ$  and thereafter at  $1^\circ$  intervals up to  $\psi = 89^\circ$ . The

collection time for each diffractogram recorded at each angle  $\psi$  was 2400 s. A low-energy solid-state germanium detector (Canberra Model GL0110) was used to record the diffractograms; and gold powder was used for system calibration. Using the series of diffractograms recorded for each specimen, the residual stress was determined as a function of depth below the surface. The stress level at a specific depth was determined from a specific set of  $\{hkl\}_\gamma$  planes; the depth being determined from the diffraction energy of the specific  $\{hkl\}_\gamma$  plane set, higher diffraction energies providing information related to deeper regions within the specimen.

The experimental setup for the angle-dispersive measurements is shown in Fig. 1b. The diffraction angle was initially  $2\theta = 37^\circ$  (denoted by the line labelled 1 in Fig. 1b) with  $\psi = 0^\circ$ . X-ray counting was performed for 15 s before moving both the source and detector by  $0.025^\circ$  towards a higher  $2\theta$  value. The process was repeated until a final  $2\theta$  value of  $40.3^\circ$  was reached (indicated by line 2 in Fig. 1b). This range of  $2\theta$  angles corresponds to d-spacings around  $d_{\{111\}_\gamma}$ . A graph of counts against  $2\theta$  was constructed to determine  $d_{\{111\}_\gamma}$  at  $\psi = 0^\circ$ . Measurements were repeated for specimen tilt values up to  $\psi = 89^\circ$ . From the results, the variation of  $d_{\{111\}_\gamma}$  could be plotted as a function of the specimen tilt angle  $\psi$ . The monochromatic radiation used for the angle-dispersive measurements had a wavelength of 0.154056 nm ( $\text{CuK}_{\alpha 1}$ ); again gold powder was used as a calibration standard.

In the angle-dispersive investigation it was decided to use  $\{111\}_\gamma$  type planes (as done in [5]) to determine the stress because of the high intensity of the  $\{111\}_\gamma$  reflections; (the  $\{111\}_\gamma$  planes were also used to determine stress at one specific depth in the energy-dispersive investigations). However it should be noted that in  $\gamma$ -based TiAl alloys the d-spacing of the  $\{111\}_\gamma$  reflections is almost identical to that of  $(0002)_{\alpha 2}$  reflections (for the Ti-49Al alloy values of  $d_{\{111\}_\gamma} = 0.233121$

nm and  $d_{(0002)\alpha_2} = 0.233075$  nm were determined from the DESY experiments that are described below). Thus great care needs to be taken in using the  $\{111\}_\gamma$  reflections to determine stress because the shift of the  $\{111\}_\gamma$  d-spacing peak could also be in part caused by stresses in the  $\alpha_2$  phase. Additionally, other  $\{hkl\}_\gamma$  reflexes that were used to determine stress using the energy-dispersive technique are close to reflexes from the  $\alpha_2$  phase. Thus it was very important to determine the respective  $\alpha_2$  and  $\gamma$  phase fractions within the samples. This was done using high-energy X-ray diffraction (HEXRD) measurements that were performed at the P07 beamline, run by HZG, at the Deutsches Elektronen-Synchrotron (DESY) in Hamburg [7]. The as-polished (unexposed) specimens, which had thicknesses ranging from 3 to 6 mm, were investigated in the transmission mode with an X-ray beam cross-section of  $300 \times 300 \mu\text{m}^2$  and a photon energy of 53.7 keV (equivalent wavelength = 0.023089 nm). The resulting Debye-Scherrer (DB) rings were recorded using a PerkinElmer XRD 1622 area detector. FIT2D software [8] was employed to azimuthally integrate the DB rings in order to convert them to intensity against  $2\theta$  diffractograms; phase fractions and lattice parameters were determined by Rietveld analysis of the diffractograms using the MAUD software package [9].

### **3 Determination of residual stress as a function of depth**

A typical energy-dispersive X-ray diffractogram is presented in Fig. 2, where it can be seen that diffraction peaks are present at certain X-ray energy values. Such a raw diffractogram must be corrected for the detector dead time, which is directly related to the experimental equipment and set-up and has an influence on the peak position. The raw diffractograms were corrected for detector dead-time as described in [10].

The determination of residual stress by X-ray diffraction relies on atomic plane spacing to determine strain; this is determined via the Bragg equation:

$$n\lambda = 2d \sin \theta \quad (1)$$

Where  $d$  is the interplanar spacing for a specific set of diffracting planes and  $2\theta$  is the diffraction angle. The wavelength  $\lambda$  is given by  $hc/E$  ( $= 1.2398/E$ ); where  $h$  (Planck's constant)  $= 4.136 \times 10^{-15}$  eV s,  $c$  (the speed of light)  $= 2.998 \times 10^8$  ms<sup>-1</sup>, and  $E$  is the energy of the diffracted beam (in keV). On substituting for  $\lambda$  in eqn. (1) and re-arranging, one obtains a relationship between the (fixed) diffraction angle ( $2\theta$ ), the X-ray energy associated to a specific diffraction peak ( $E_{hkl}$ ) and the corresponding  $d$ -spacing of the diffracting plane  $d_{hkl}$ :

$$d_{hkl} \text{ (in nm)} = 0.6199 / (\sin \theta \times E_{hkl} \text{ (in keV)}) \quad (2)$$

For example, using eqn. (2) it is possible to show that for an un-strained  $\gamma$  TiAl lattice, with lattice parameters:  $a = 3.975$  nm,  $c = 4.068$  nm [11] and a fixed diffraction angle ( $2\theta$ ) of  $16^\circ$ , the X-ray energy of the  $\gamma_{\{111\}}$  diffracting planes will be at around 19.2 keV, as can be seen in Fig. 2. In order to determine the residual stress distribution from the surface towards the bulk material, it is necessary to evaluate how the X-ray energy of the diffraction peaks of the different sets of diffracting planes varies as a function of the specimen tilt angle  $\psi$  (the angle defined by  $\psi$  in Fig. 1). The variation of the diffraction peak energy for the  $\{111\}_\gamma$  planes with increasing specimen tilt angles ( $\psi$ ) and the associated values of  $d_{\{111\}_\gamma}$ , calculated from the diffraction peak energies using eqn. (2), is indicated in Fig. 3a for the as-polished Ti-49Al specimen. In some cases, particularly at high tilt angles ( $\psi$ ), the peaks are difficult to evaluate due to an insufficient number of counts. Data points from such peaks have not been used in the residual stress

calculations. This procedure has been repeated for different types of diffracting planes, and graphs such as that shown in Fig. 3a were obtained for the different types of  $\{hkl\}_\gamma$  planes. As the data shows a linear trend, the classical  $\sin^2\psi$  method introduced by Macherauch and Müller [12] can be used to determine the residual stress; which was done independently for the individual types of crystallographic planes  $\{hkl\}_\gamma$ . The stress is determined from the gradient of graphs such as that shown in Fig. 3a using the equation:

$$\sigma = \frac{1}{d_0^{hkl}} \frac{m}{\frac{1}{2}S_2^{hkl}} \quad (3)$$

where  $\sigma$  is the near-surface residual stress parallel to the surface (see Fig. 1 for its direction) determined for specific  $\{hkl\}_\gamma$  planes;  $d_0^{hkl}$  is the d-spacing of the  $\{hkl\}_\gamma$  lattice planes in an unstrained lattice,  $m$  is the gradient of the regression line fitted through the d-spacing against  $\sin^2\psi$  data (Fig. 3a), and  $\frac{1}{2}S_2^{hkl}$  is a so called ‘‘X-ray elastic constant’’. The stress  $\sigma$  determined in this way for single phase materials is often termed macrostress, or type I stress, and assumed to be homogeneous over a large number of grains. In multi-phase materials where the different phases could impose stress on each other due to different thermal expansion coefficients, for example, the residual stresses determined are known as ‘‘pseudo-macro stresses’’ (p-m stresses) or ‘‘phase-homogeneous’’ stresses. As the value of  $d_0^{hkl}$  in eqn. (3) is unknown, it has to be approximated. Since the sampled volume is confined to a thin surface layer defined by the irradiated area and the penetration depth it is assumed to be under a biaxial stress state, with no stress in the direction perpendicular to the surface. Under these conditions the value  $d_0^{hkl}$  can be approximated. For any set of planes this is done by obtaining the value of the d-spacing from data plotted in the relevant d-spacing against  $\sin^2\psi$  plot (Fig. 3a for the 111 planes) Fig. 3a at the value of  $\sin^2\psi$  corresponding to:

$$\frac{-2s_1^{hkl}}{\frac{1}{2}s_2^{hkl}} \quad (4)$$

The values of  $s_1^{hkl}$  and  $\frac{1}{2}s_2^{hkl}$  are determined by the type of planes, the crystal lattice, the single crystal elastic constants and the specific stress-strain interaction model employed. In the present study the single-crystal elastic constants ( $c_{ij}$ ) and lattice parameters determined for  $\gamma$ -TiAl at room-temperature (298 K) by Tanaka et al. [11] have been used. Equivalent elastic compliances ( $s_{ij}$ ) can be determined using the equations given in [13]. Classically, the elastic stress-strain interaction has been described by two models; the Voigt (homogeneous strain) [14] and Reuss (homogeneous stress) [15] models, that apply for two extreme cases of stress-strain behaviour. Another model that is often used to determine the relationship between stress and strain is the Kröner model [16], which has been used in the present study because it closely approximates the real-world situation. Equations to calculate  $s_1^{hkl}$  and  $\frac{1}{2}s_2^{hkl}$  for the different models are given by Behnken and Hauk [17]; the free software of Manns and Scholtes described in [18] can be used to determine their values.

Once the residual stress has been obtained for each type of lattice plane from graphs such as that shown in Fig. 3a and using eqn. (3), it is necessary to determine the depth to which this stress is associated. As can be seen in Fig. 2, and is described by eqn. (2), lattice planes with smaller d-spacing diffract at higher X-ray energies. Such X-rays penetrate deeper into the specimen than those associated with planes of larger d-spacing. Thus the stress determined from high-index lattice planes (small d-spacing) is associated to material that is distributed to deeper regions below the surface. The depth of X-ray penetration also depends on the diffraction angle ( $2\theta$ , which remains constant for the energy-dispersive technique) and the specimen tilt angle ( $\psi$ ) at

which each specific energy-dispersive diffractogram was recorded. The X-ray penetration (information) depth ( $\tau$ ) for the current energy-dispersive set-up is given by:

$$\tau = \frac{\sin \theta \cos \psi}{2\mu(E^{hkl})} \quad (5)$$

$\mu(E^{hkl})$  is the X-ray linear absorption coefficient for the alloy at the diffraction energy for each specific type of  $\{hkl\}$  plane.  $\tau$  represents the thickness of a surface layer that contributes to around 63.2 % (1-1/e) of the diffracted intensity. As explained above, the stress from a specific set of planes is determined from the slope of the d-spacing against  $\sin^2 \psi$  plot (Fig. 3a for the 111 planes). From eqn. (5) it can be seen that for any set of planes the penetration (information) depth has a maximum at  $\psi = \psi_{min} = 0^\circ$  and a minimum for the highest value of  $\psi$  ( $\psi_{max}$ ) used in the d-spacing against  $\sin^2 \psi$  plot. As the stress is determined from the slope of the plot, it is consequently related to a depth that is somewhere between these extreme values; by convention it is assigned to the mean penetration (information) depth, given by Denks and Genzel [10] as:

$$\tau_{hkl} = \frac{\tau_{hkl(\psi=\psi_{min})} + \tau_{hkl(\psi=\psi_{max})}}{2} \quad (6)$$

A limitation of the energy-dispersive setup used in this study is that information very close to the surface was not accessible; this is the reason why the angle-dispersive technique was also employed. The variation of  $d_{\{111\}_\gamma}$  against  $\sin^2 \psi$  plotted from the angle-dispersive measurements is seen in Fig. 3b. The curved shape of the plot, especially at high values of  $\sin^2 \psi$ , results from high non-linear surface stresses. The ‘‘universal plot’’ procedure [19] was thus used to obtain the stress profiles. The value of  $d_0^{hkl}$  is interpolated from the two data points adjacent to the value of  $\sin^2 \psi$  given by eqn. (4) for the  $\{111\}_\gamma$  planes. The stress for each individual point on the  $d_{\{111\}_\gamma}$  against  $\sin^2 \psi$  graph is then calculated using the equation:

$$\sigma = \frac{\varepsilon_{\psi}^{hkl}(\tau)}{1/2s_2^{hkl} \sin^2 \psi + 2s_1^{hkl}} = \frac{\left[ \frac{d_{(\psi)}^{hkl} - d_0^{hkl}}{d_0^{hkl}} \right]}{1/2s_2^{hkl} \sin^2 \psi + 2s_1^{hkl}} \quad (7)$$

Where  $d_{(\psi)}^{hkl}$  is the d-spacing for each individual data point on the graph,  $d_0^{hkl}$  is interpolated (described above) and the value of  $\sin^2 \psi$  is obtained from the specimen tilt angle at each specific data point. It should be noted that stresses were only calculated for data points with values of  $\sin^2 \psi$  that are significantly larger than the value of  $\sin^2 \psi$  in the strain-free direction (i.e. those above 0.5 – 0.6 in the present case for  $\{111\}$  planes). The depth of X-ray penetration  $\tau$  (information depth) has been obtained using eqn. (5) but with  $\mu(E^{hkl})$  having a constant value (= 562 cm<sup>-1</sup>) due to the monochromatic nature of the X-rays used.

#### 4 Results and Discussion

It is firstly important to establish that the stress measurements reflect the stress within the  $\gamma$  phase, and have not been significantly influenced by the  $\alpha_2$  phase. Macroscopic specimen volumes of both alloys in the un-exposed (as-polished) condition were investigated by transmission HEXRD (at DESY). The diffraction patterns obtained showed relatively smooth and continuous Debye-Scherrer rings and indicated that there was no texture in Ti-49Al and only a weak texture in Ti-45Al-5Nb-0.2B-0.2C. After integrating over the diffraction rings, Rietveld refinement was used to determine the  $\alpha_2$  phase fraction in each alloy. The results indicate that the  $\alpha_2$  phase content in the Ti-49Al and Ti-45Al-5Nb-0.2B-0.2C alloys were 1.2% and 11.5% respectively. The small volume fraction of  $\alpha_2$  phase in Ti-49Al is also apparent from the very low intensity of  $\alpha_2$  peaks in the energy-dispersive diffractogram shown in Fig. 2. Assuming a random texture (commonly known as “texture-free”) and equal phase fractions, diffraction pattern simulation calculations indicate that the intensity of the  $\alpha_2$  (0002) peak is only 54.6 % of that of

the  $\gamma$  {111} peak. As a result only 0.7 % and 6.3 % of the intensity of the  $\gamma$  {111} peak for the Ti-49Al and Ti-45Al-5Nb-0.2B-0.2C alloys in the stress measurements originates from the  $\alpha_2$  phase. From these findings it therefore seems justified to assign the results from the stress measurements to the behaviour of the  $\gamma$  phase, in particular for the Ti-49Al alloy, but also for the weakly textured Ti-45Al-5Nb-0.2B-0.2C alloy.

The variation of residual stress as a function of depth, determined using the Kröner model, for the as-polished (un-exposed) and exposed Ti-49Al and Ti-45Al-5Nb-0.2B-0.2C specimens is shown in Fig. 4. The general trend for the as-polished specimens is similar for both alloys with a high compressive stress being present near to the surface, which diminishes with increasing depth to levels of around -200 MPa at 80  $\mu\text{m}$  below the surface. It is interesting to note that the maximum compressive stress developed within the Ti-49Al specimen ( $\approx$  -900 MPa) is significantly higher than that in the Ti-45Al-5Nb-0.2B-0.2C specimen ( $\approx$  -450 MPa). The residual stress probably arises as a result of work hardening from plastic deformation that took place during cutting, but also possibly during specimen grinding/polishing. This is not surprising as it is known that cutting and surface preparation can play a significant role in determining the residual surface stress of TiAl [4] and materials in general.

Although the residual stress-depth trends are similar, the stress-depth profiles for the two un-exposed alloys are rather different. For the high strength Ti-45Al-5Nb-0.2B-0.2C alloy, the compressive stress reduces from -450 MPa in the near-surface layers by around 250 MPa to -200 MPa at a depth of around 80  $\mu\text{m}$ . This behaviour is quite unlike that of the softer un-exposed Ti-49Al alloy, where the reduction of compressive stress between the near-surface and a depth of 80  $\mu\text{m}$  is more significant, reducing by about 700 MPa to -200 MPa. These differences are probably related to the different strength levels of the alloys, it being observed that residual stress after

plastic deformation via shot peening penetrates deeper into softer material [20]. One could ask whether the different phase fractions within the two alloys plays a role with respect to the residual internal stresses of the unexposed materials. X-ray diffraction studies [21-23] performed on compressively deformed ( $\alpha_2+\gamma$ ) alloys have indeed demonstrated that significant residual tensile stresses develop in the  $\alpha_2$  phase, which are compensated by residual compressive stresses in the  $\gamma$  phase. The level of these residual stresses is expected to increase with the total deformation. As the softer Ti-49Al alloy is most probably deformed to a higher strain by cutting and grinding, the residual stresses developed could be higher than those within the harder Ti-45Al-5Nb-0.2B-0.2C alloy. The details of elasto-plastic co-deformation of the  $\gamma$  and  $\alpha_2$  phases are very complex because the isolated  $\gamma$  and  $\alpha_2$  phases exhibit significant plastic anisotropies. In lamellar colonies the shear anisotropy is further exacerbated because the two phases are aligned according to crystallographic orientation relationships [24]. Thus, the level of residual stresses depends on the mutual orientation of the  $\gamma$  and  $\alpha_2$  phases. In particular, high residual tensile stresses are expected in the  $\alpha_2$  phase, when it is oriented in a way that makes prismatic slip impossible (which is the only slip variant which can be activated with relative ease at room temperature) and it is constrained by  $\gamma$  phase that is easily deformable by slip of ordinary  $1/2\langle 110 \rangle$  dislocations. Possible mechanisms for the strain accommodation between the two phases have been discussed in [25, 26]. For a better understanding, the phase stresses should be determined independently.

In Fig. 4a it can be seen that there is a relatively large step in residual stress values on moving from the wavelength to angle-dispersive determined results; the reason for this is unknown. The influence of  $(0002)_{\alpha_2}$  reflections, which could interfere with the  $\{111\}_{\gamma}$  reflections, and thus all stress results obtained, can be excluded because the Ti-49Al alloy contains almost no  $\alpha_2$  phase, as

explained earlier. A smaller step is also apparent in the stress profile of the as-polished Ti-45Al-5Nb-0.2B-0.2C specimen. For both exposed specimens there is a relatively smooth transition between the stress values determined using the different techniques.

Similar levels of residual stress near the surface and at 100  $\mu\text{m}$  depth, -700 MPa and -200 MPa respectively, have been determined for a powder metallurgy based Ti-47Al-2Cr-2Nb alloy after turning [4]. That study also indicated that grinding resulted in a somewhat lower residual stress (-400 MPa near-surface and -180 MPa at 100  $\mu\text{m}$  depth) compared to turning. In the context of the current study this indicates that the residual stress levels of the as-polished (un-exposed) specimens are comparable to those developed during turning and that the stress levels have not been significantly reduced despite careful grinding and vibration polishing. The stresses are quite likely comparable to those present at the surface of carefully prepared tensile test specimens and thus closely approximate the actual near-surface residual stress conditions prior to embrittlement.

It is clear from Fig. 4 that exposure at 700°C for only one hour has led to a significant reduction of the overall residual stress in both alloys and the development of tensile stress in the layer of material within 0.6  $\mu\text{m}$  from the outer surface. The trend in the reduction of this tensile near-surface residual stress towards the bulk is similar for the two alloys. After exposure the residual stress at a depth of 1  $\mu\text{m}$  remains compressive but has been reduced in absolute value by around 700 MPa in Ti-49Al and around 350 MPa in the Ti-45Al-5Nb-0.2B-0.2C alloy. These correspond to reductions in absolute stress of over 80 % for both alloys. For the exposed Ti-49Al specimen the compressive stress reaches a maximum of about -200 MPa between 2 and 10  $\mu\text{m}$  from the surface and then reduces in magnitude to almost zero at a depth of 80  $\mu\text{m}$ . In the exposed Ti-45Al-5Nb-0.2B-0.2C specimen the stress level between 4 and 80  $\mu\text{m}$  is almost constant at around -100 to -150 MPa and is similar to that of the un-exposed alloy at a depth of around 80  $\mu\text{m}$ .

As the compressive residual stress prior to exposure is a consequence of near-surface plastic deformation and work hardening during specimen preparation, a relevant understanding of how thermal treatments affect work hardening and thus the development of residual stress after exposure would be useful. The recovery of work hardening via thermal treatment has been studied extensively by Appel et al. [27]. On loading to above the elastic limit, deformation preceded via the glide of ordinary dislocations and a limited degree of order twinning. Various mechanisms contributed to the room-temperature work hardening but high-temperature exposure led to significant recovery, due to the annealing out of short-range deformation induced obstacles, and consequently a significant reduction of the flow stress. Additionally, Lindemann et al. [20], using the hole-drilling method, observed that the near-surface residual compressive stress in a shot-peening TiAl specimen was reduced at a depth of 100  $\mu\text{m}$  from between -500 to -600 MPa to around -100 MPa by annealing for 50 h at 650°C. This effect had serious consequences on the subsequent room-temperature fatigue behaviour of the shot-peened material, where, after thermal exposure the enhanced fatigue properties were significantly reduced [20]. The reduction of near-surface compressive stress levels in the fatigue specimens after exposure was believed to result from the annealing out of deformation-induced dislocations obstacles.

Interestingly, for both alloys, the results in Fig. 4 indicate that a tensile stress has developed close to the outer surface after cooling from the exposure temperature. Unfortunately, from this investigation it is not possible to identify at what stage during the exposure/cooling cycle the tensile stress developed. For both alloys the transition from compressive to tensile stress takes place about 0.6  $\mu\text{m}$  from the outer surface and increases to values of around +300 to +350 MPa at a distance of 0.15  $\mu\text{m}$  from the surface. This finding supports that of Wu et al. [5] who showed that a 250 MPa tensile stress developed after exposure (in their case 2 h at 700°C) within a 2  $\mu\text{m}$

thick layer below a nm thick oxygen enriched surface layer. Such an ultra-thin layer, saturated with up to 2 at. % oxygen, has been observed in the  $\gamma$  phase (using X-ray photoemission spectroscopy) after the initial stages of oxidation at 650°C under low pressure oxygen [28]. After oxygen saturation of the  $\gamma$  phase, alumina starts to form, and a nm-thick sub-alumina layer starts to develop. This layer, between the alumina and base material, was depleted by up to 25 at. % Al and arose due to alumina formation, which requires the outward diffusion of Al atoms. The variation of the  $\gamma$  phase lattice parameters in binary alloys has been presented in [29] for alloys containing 48.5 to 55 at. % Al. Using this data, and extrapolating it to 46 at. % Al, it is possible to determine the variation of the  $\{111\}_\gamma$  d-spacing as a function of composition from 46 to 55 at. % Al. The  $\{111\}_\gamma$  d-spacing increases from 0.232971 nm to 0.233383 nm when the Al content of the  $\gamma$ -phase reduces from 49 to 46 at. %. Using Hooke's law and the relevant crystallographic Young's modulus of 203.1 GPa for elastic deformation normal to the  $\{111\}_\gamma$  planes (obtained using the Kröner model with the crystal constants given in [11]), it can be calculated that such an increase in d-spacing corresponds to a 359 MPa tensile stress. As the slightly larger lattice of any ultra-thin aluminium-poor (46Al)  $\gamma$  phase is situated above the Al-rich (49Al) base material, it would be forced into compression, and would exert a tensile stress into the material below. Although it is difficult to estimate the magnitude of any stresses developed, it is interesting to note that the value of 359 MPa is similar to the residual stress values at a depth of 0.15  $\mu\text{m}$ . It should however be emphasised that in the present study the presence of any such nanoscale difference in composition was not investigated, although other work [28] has shown the development of such features. While the exact mechanism responsible for the development of the tensile stress is unknown, it is speculated to be due to nanoscale compositional changes at the

surface, such as described above, that transmit stress into deeper regions, on the order of a micron or so, within the material.

With regard to embrittlement, the retention of significant compressive residual stress both at and immediately below the surface would certainly seem beneficial in suppressing fracture. Indeed, it has been reported that ductility is restored in exposed tensile specimens by shot peening [5]. Similarly, it has been widely reported that ductility is recovered after removal of the exposed surface by grinding/polishing. Both these processes restore compressive stress into the surface and, at the same time, may remove potentially chemically altered surface material that is under tensile stress. In the shot-peening study [20], the relevance of near-surface compressive stresses on fatigue behaviour was clearly demonstrated. It was shown that near-surface compressive stresses shift crack initiation away from the surface to the specimen interior, which resulted in a substantial improvement of fatigue strength. Thus, it could be speculated that the reduction of such relatively long-range stresses during exposure is the main origin of environmental embrittlement. In contrast, it appears questionable if the short-range stress field arising from the tensile stress developed in the 0.6  $\mu\text{m}$  thick outer layer could induce failure. Of course, cracks may prematurely nucleate in this sub-surface region at lower external loading stresses compared to un-exposed specimens. However, in order to initiate failure such cracks must be at least as long as the critical crack length. This length ( $a_c$ ) depends on the applied stress and is given by  $a_c = K_{1c}^2/(\pi\sigma^2)$ . Assuming a low fracture toughness of  $K_{1c} = 10 \text{ MPa m}^{1/2}$  [30] and a stress of +900 MPa, then the critical crack length is 39  $\mu\text{m}$ . This crack length is much longer than the depth of the tensile stress field that is developed after exposure.

In order to clarify the effect of reduced near-surface compressive residual stress on ductility it would be interesting to test tensile specimens that have been either heavily electro-polished, or prepared by electro-chemical milling. Of course it cannot be ruled out that electro-

polishing/chemical milling may lead to chemical based effects which themselves cause embrittlement. In work by Wu et al. [31] it was clearly demonstrated that the stress level at which the first pre-yield cracking occurred, was strongly influenced by the surface residual stress. Interestingly, the development of near-surface tensile residual stress was not observed in that study; however, the depth resolution of the measurements (50  $\mu\text{m}$ ) would have been far too coarse to identify similar tensile residual stresses to those found in the present investigation. One observation that may seem to indicate that residual stress very deep within the material plays only a minor role in embrittlement is that tensile specimens of a high strength TNB-V2 alloy made from blanks that had been heat-treated at 800°C for 1504 h and then furnace cooled, showed no loss of room-temperature ductility [32]. This of course assumes that any residual stresses are significantly reduced during such a long-term treatment and that no significant stresses are developed between microstructural constituents or phases during furnace cooling. Near surface compressive stresses would certainly have been developed during specimen manufacture via turning/grinding.

An aspect that is not widely discussed in the TiAl literature is the relationship between alloy strength and the severity of embrittlement. Even after short-term exposure, high-strength alloys typically break at stresses below the yield stress whereas low to medium strength alloys exhibit plastic elongations that are typically only reduced to around 50% of those for un-exposed specimens. This observation could be somehow related to the critical defect length required for fracture. As discussed in ref. [33] with specific reference to TiAl, for a given value of fracture toughness, the critical defect size is reduced for high strength alloys. From the current investigation it is apparent that even before starting a tensile test, a compressive stress of up to -900 MPa exists in the near-surface material of an un-exposed Ti-49Al specimen, and -400 MPa in a Ti-45Al-5Nb-0.2B-0.2C specimen. After exposure, even before testing, residual tensile

stresses of around +300 to +350 MPa are present 0.15  $\mu\text{m}$  from the surface, and an overall tensile residual stress is present within 0.6  $\mu\text{m}$  from the surface in both the high and low-strength alloys. It is likely that even higher tensile stresses are present closer than 0.15  $\mu\text{m}$  to the surface. On loading an exposed tensile specimen to an overall tensile stress of +400 MPa, the results in Fig. 4 seem to indicate that the tensile stress present 0.15  $\mu\text{m}$  from the surface will be around +700 to +750 MPa (maybe even higher closer to the surface). For an un-exposed Ti-49Al specimen under a similar global stress, a compressive stress would exist in the outer 30  $\mu\text{m}$ , and tensile stress would only be present further away from the surface. For an un-exposed Ti-45Al-5Nb-0.2B-0.2C specimen under a global imposed stress of +400 MPa, the near-surface layers would experience little stress and a tensile stress of around +200 MPa is likely to be present 80  $\mu\text{m}$  from the outer surface. As mentioned earlier, the very high local near-surface tensile stresses present in exposed specimens on loading will certainly aid crack initiation. It is interesting that acoustic emission during tensile testing, reportedly resulting from crack formation/propagation [5], took place at stress levels 200 to 300 MPa lower in exposed compared to un-exposed specimens. This observation is consistent with the presence of near-surface tensile residual stress after exposure; but it should be noted that the acoustically registered events did not result in specimen failure. As described earlier, once a crack has formed, its length, the local stress level and the fracture toughness will determine if it remains stable or propagates causing fracture. For cracks which prematurely initiate during tensile testing of exposed low strength specimens due to the tensile surface stress, it could be argued that due to their low strength the overall stress level is sufficiently low that failure does not take place, and hence some ductility is measureable. If cracks are initiated in the high-strength alloys, then the higher overall stress level reached before the high-strength alloy starts to yield would lead to a shorter critical crack length. However after crack initiation and growth into the sub-surface, such cracks would experience a reduced stress

level and would seem unlikely to lead to failure, unless the external stress was further increased to above that required for the initiated crack to cause fracture. Thus, it is unclear if the short-range near-surface tensile residual stress and reduced state of compressive stress deeper away from the surface after exposure are responsible for post-exposure embrittlement. Fracture mechanic modelling studies aimed towards clarifying the situation with regard to residual surface tensile stress, overall stress and catastrophic fracture would certainly be beneficial in helping to clarify the situation.

## **5 Conclusions**

Residual stress has been determined as a function of depth in as-polished specimens before and after exposure in air at 700°C/1 h. It was found that high compressive stresses were present in the near-surface region of as-polished samples, despite careful preparation. The un-exposed low-strength alloy had a maximum compressive residual stress of around -900 MPa very close to the surface, compared to about -450 MPa for the high strength alloy. In both alloys the residual stresses 80 µm from the surface were similar at around -200 MPa. After exposure the residual stress profiles were similar with a tensile stress developing within the initial 0.6 µm from the surface and a relatively low compressive residual stress in the underlying material. It has been postulated that the post-exposure embrittlement of TiAl may be related to a reduction of overall near-surface compressive stress due to annealing out of deformation induced obstacles. This stress can be restored by post-exposure grinding or peening, both of which restore ductility. It remains unclear if the short-range near-surface tensile residual stress, that is developed after exposure and which confirms previous findings [5], is responsible or contributes to post-exposure embrittlement.

## Acknowledgements

The authors would very much like to thank M. Klaus and C. Genzel (both Helmholtz Zentrum Berlin) for performing the stress profile measurements and providing the stress profile data. Additional thanks go to S. Gayer for performing, and N. Schell and P. Staron for enabling phase fraction measurements to be made using the P07 beamline at DESY. Other colleagues including U. Fröbel, U. Lorenz, D. Matthiessen, F-P. Schimansky, and A. Stark are thanked for helpful discussions and/or provision of material.

## References

1. Bewlay BP, Weimer M, Kelly T, Suzuki A and Subramanian PR. In: Baker I, Heilmaier M, Kumar S, and Yoshimi K, editors. Intermetallic-based alloys - science, technology and applications. Materials Research Society symposium proceedings, vol. 1516. Warrendale (PA): MRS, 2013, pp. 49–58.
2. Dowling WE and Donlon WT, *Scripta Metall Mater* (1992), 27, pp. 1663-1668.
3. Austin CM and Kelly TJ. In: Darolia R, Lewandowski JJ, Liu CT, Martin PL, Miracle DB and Nathal MV, editors. *Structural Intermetallics*. Warrendale (PA): TMS, 1993, pp. 143-150.
4. Thomas M, Berteaux O, Popoff F, Bacos M-P, Morel A, Passilly B, and Ji V, *Intermetallics* (2006), 14, pp. 1143-1150.
5. Wu X, Huang A, Hu D, and Loretto MH, *Intermetallics* (2009), 17, pp. 540-552.
6. Draper SL, Lerch BA, Locci IE, Shazly M, and Prakash V, *Intermetallics* (2005), 13, pp. 1014-1019.
7. Schell N, King A, Beckmann F, Müller M, and Schreyer A, *Material Science Forum* (2014), 772, pp. 57-61.

8. Hammersley A.P, Svensson SO, Hanfland M, Fitch AN, and Häusermann D, High Pressure Research (1996), 14, pp. 235-248.
9. Lutterotti L, Bortolotti M, Ischia G, Lonardelli I, and Wenk H-R, Z Krist Suppl (2007), 26, pp. 125-130.
10. Denks IA and Genzel Ch, Nucl Instr and Methods in Phys Res B (2007), B262, pp. 87-94.
11. Tanaka K, Ichitsubo T, Inui H, Yamaguchi M, and Korwa M, Phil Mag Letters (1996), 73, pp. 71-78.
12. Macherauch E and Müller P, Z Angew Phys (1961), 13, pp. 305-312.
13. Bollato A. *Poisson's ratio for tetragonal crystals*. Technical report ARL-TR-423 (March 1995), US Army Research Laboratory, Electronic and Power Sources Directorate.
14. Voigt W, Lehrbuch der Kristallphysik. Berlin/Leipzig: Teubner (1928), p. 962.
15. Reuss A, Z Angew Math u Mech (1929), 9, pp. 49-58.
16. Kröner E, Z Phys (1958), 151, pp. 504-518.
17. Behnken H and Hauk V, Z Metallkde (1989), 77, pp. 620-626.
18. Manns T and Scholtes B, HTM J. Heat Treatm Mat (2010), 65 (2), pp. 75-84.
19. Ruppertsberg H, Detemple I and Krier J, Phys stat sol (a) (1989), 116, pp. 681-687.
20. Lindemann J, Buque C and Appel F, Acta Mater (2006), 54, pp. 1155-1164.
21. Riemer M, Biermann H, Kowaleski R, and Mughrabi H. In: Nathal MV, Darolia R, Liu CT, Martin PL, Miracle DB, Wagner R, and Yamaguchi M, editors. Structural Intermetallics 1997, Warrendale (PA): TMS, 1997, pp. 305-312.
22. Riemer M, Jentsch HG, Biermann H, and Mughrabi H, Intermetallics (1999), 7, pp. 241-249.

23. Guo FA, Ji V, Zhang YG, Chen CQ. *Mater Sci Eng* (2003), A341, pp. 182-188.
24. Blackburn MJ. In: Jaffee RI, Promisel NE, editors. *The science, technology and application of titanium*. Oxford: Pergamon Press, 1970, pp. 633-643.
25. Paul JDH, Hoppe R and Appel F, *Acta Mater* (2016), 104, pp. 101-108.
26. Hoppe R and Appel F, *Acta Mater* (2014), 64, pp. 169-178.
27. Appel F, Sparka U and Wagner R, *Intermetallics* (1999), 7, pp. 325-334.
28. Maurice V, Despert G, Zanna S, Josso P, Baco MP, and Marcus P, *Acta Mater* (2007), 55, pp. 3315-3325.
29. Pfullmann T, Beaven PA, *Scripta Metall Mater* (1993), 28, pp. 275-280.
30. Appel F, Paul JDH and Oehring M, *Gamma titanium aluminides - science and technology*. Weinheim, Germany: Wiley-VCH (2011), p. 378.
31. Wu X, Hu D, Preuss M, Withers PJ, and Loretto MH, *Intermetallics* (2004), 12, pp. 281-287.
32. Ref. 30, p. 452.
33. Ref.30, p. 392.

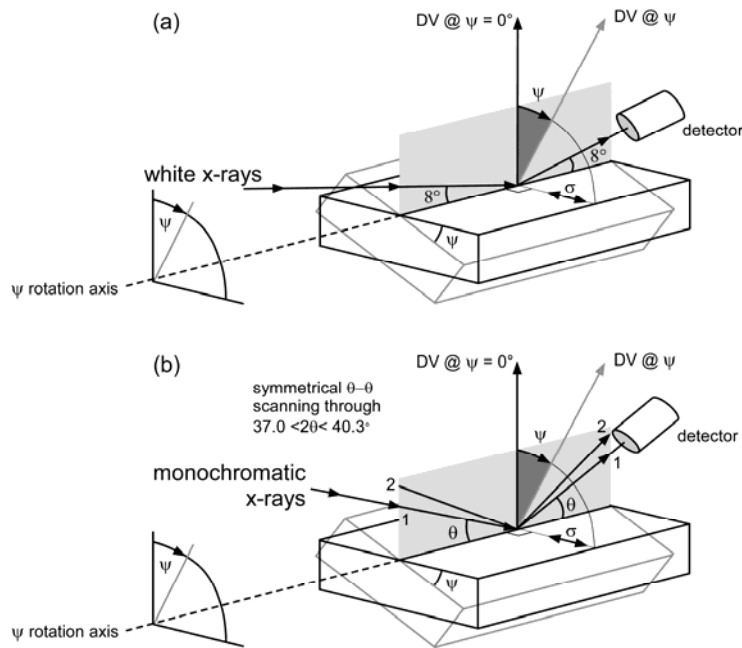


Fig. 1: Schematic diagrams showing the experimental set-up for (a) energy-dispersive (white X-rays) and (b) angle-dispersive (monochromatic X-rays) diffraction. In (a) the X-ray incidence and detector take-off angles were fixed at  $8^\circ$  ( $2\theta = 16^\circ$ ). As the specimen is tilted through the angle  $\psi$  ( $0^\circ$  to  $89^\circ$ ), the diffraction vector (DV) of the diffracting planes also tilts, as shown in the diagram. In (b) the diffraction angle was initially  $2\theta = 37^\circ$  (indicated by line 1) and  $\psi = 0^\circ$ . X-ray counting was performed stepwise by moving the source and detector until a final  $2\theta$  value of  $40.3^\circ$  was reached (indicated by line 2); various specimen tilt angles up to  $\psi = 89^\circ$  were used. The residual stress was determined in the direction indicated by  $\sigma$  in Figs. 1a and b; which for the extruded specimens is parallel to the extrusion direction.

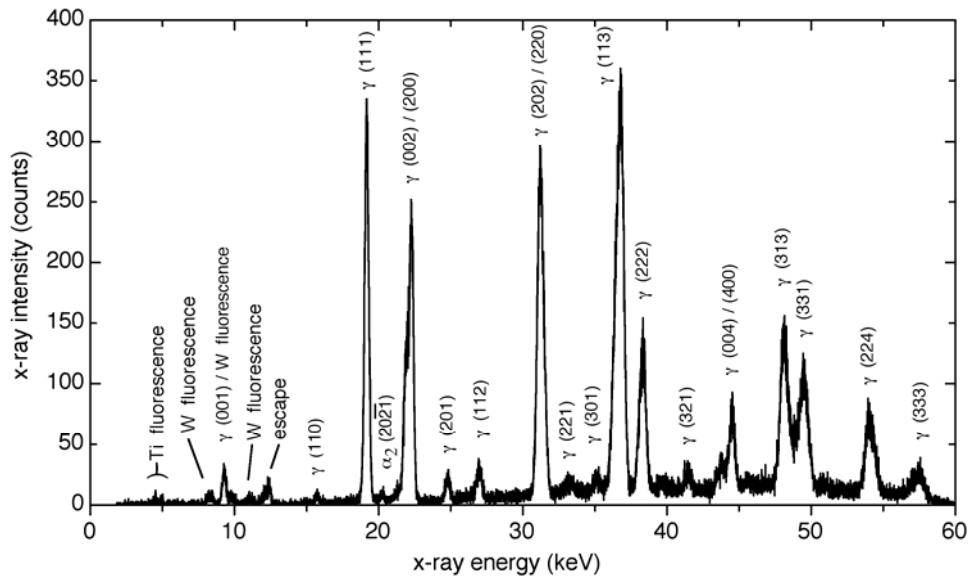


Fig. 2: Raw (uncorrected) energy-dispersive diffractogram collected from the as-polished (unexposed) Ti-49Al specimen at an angle of  $\psi = 0^\circ$ . The diffraction peaks for the  $\gamma$ -TiAl phase have been labelled. It is important to note that the strongest reflection for the  $\alpha_2$ -phase belongs to  $\{20 \bar{2}1\}_{\alpha_2}$  planes (also labelled). This reflection is only just detectable in the diffractogram, indicating that the specimen is composed of almost 100%  $\gamma$ -phase (in agreement with the HEXRD findings) in this randomly textured powder based specimen.

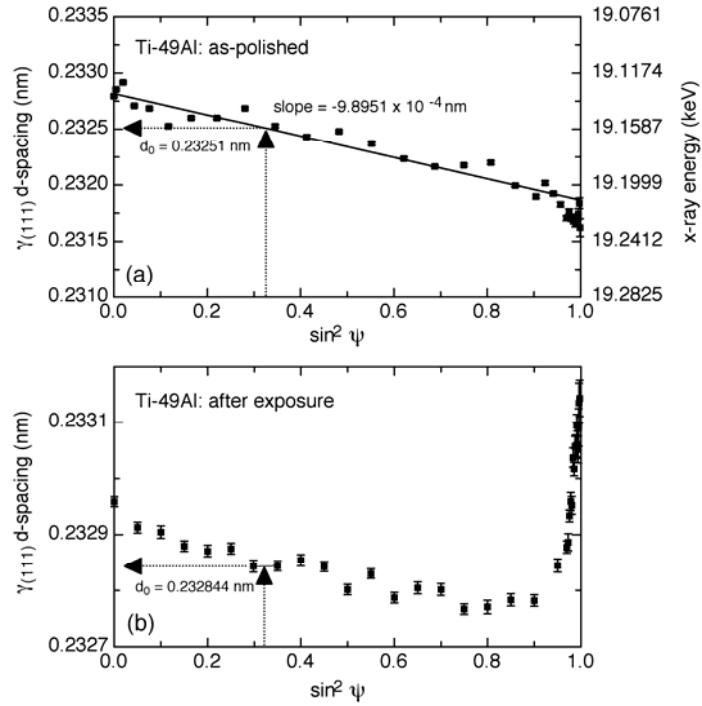


Fig. 3(a): Graph showing the variation of the  $\gamma_{\{111\}}$  plane d-spacing (determined by energy-dispersive diffraction) with  $\sin^2\psi$  for the as-polished (un-exposed) Ti-49Al alloy. The slope of the line through the data is  $-9.8951 \times 10^{-4}$  nm. Using the Kröner model values of  $s_1^{III}$  and  $\frac{1}{2}s_2^{III}$  calculated from the software in [18] ( $-9.46 \times 10^{-7}$  and  $5.87 \times 10^{-6}$  MPa $^{-1}$  respectively), the value of  $\sin^2\psi$  at  $d_{0\{111\}\gamma}$  (determined using eqn. (4)) is 0.322317. The corresponding  $\{111\}_{\gamma}$  d-spacing ( $d_{0\{111\}\gamma}$ ) at this value of  $\sin^2\psi$  is 0.23251 nm. This value of  $d_{0\{111\}\gamma}$  is used together with the gradient of the line through the data ( $m = -9.8951 \times 10^{-4}$  nm) and the value of  $\frac{1}{2}s_2^{III}$  to obtain the residual stress ( $\approx -725$  MPa) using eqn. (3). Such graphs have also been obtained for other  $\{hkl\}_{\gamma}$  planes to obtain the residual stress at other depths.

Fig 3(b): Variation of the  $\{111\}_{\gamma}$  plane d-spacing (determined by angle-dispersive diffraction) with  $\sin^2\psi$  for the Ti-49Al alloy after exposure. The high residual stress gradient near the surface results in a strong increase of the  $d_{\{111\}\gamma}$  values at high values of  $\sin^2\psi$ . The stress is determined for the individual points on the graph using eqn. (7), and the related depth is given by eqn. (5).

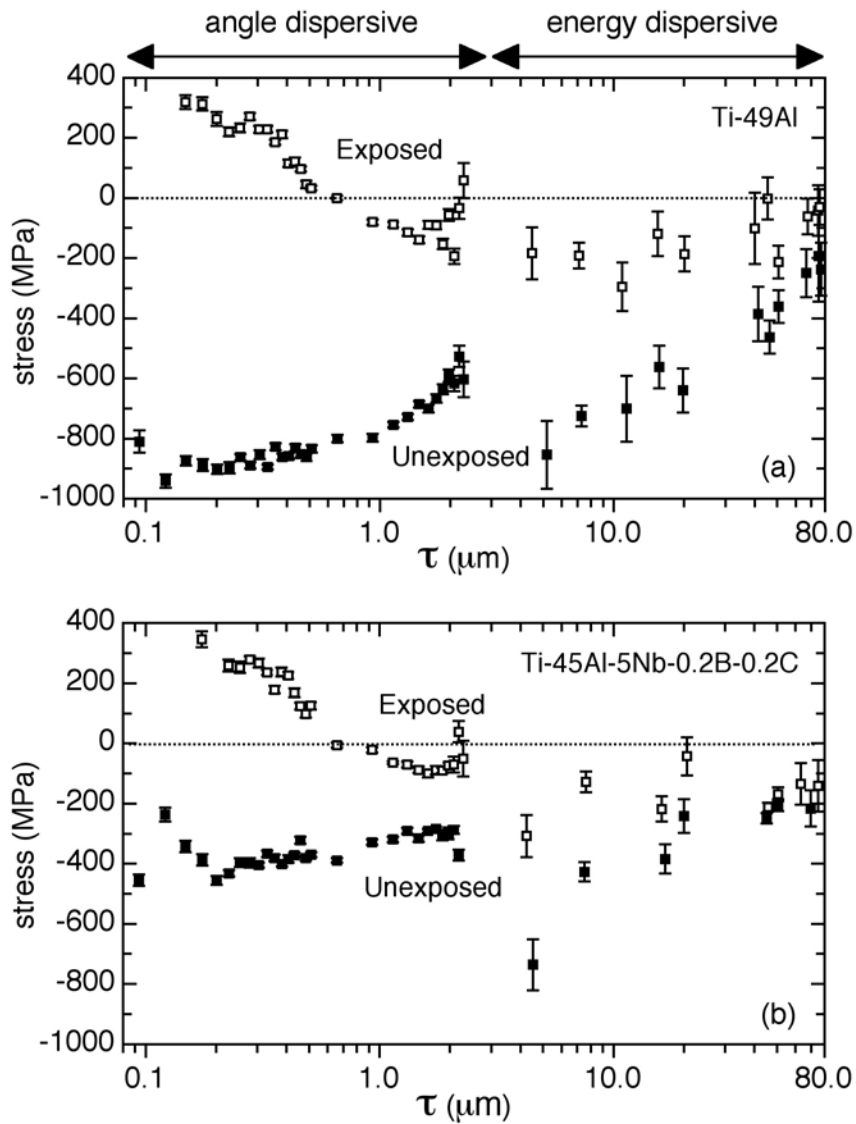


Fig. 4: Graphs that compare the near-surface residual stress profiles in un-exposed (as-polished) and exposed ( $700^{\circ}\text{C}/1 \text{ h}$ ) specimens of (a) Ti-49Al and (b) Ti-45Al-5Nb-0.2B-0.2C. As indicated at the top of the figure, stresses for points on the left hand side of the graphs were determined using angle-dispersive diffraction and those on the right using energy-dispersive diffraction.